Eastward-Propagating Disturbances in the Tropical Pacific

LIDIA HUAMAN AND COURTNEY SCHUMACHER

Department of Atmospheric Sciences, Texas A&M University, College Station, Texas

GEORGE N. KILADIS

NOAA/Earth System Research Laboratory, Boulder, Colorado

(Manuscript received 29 January 2020, in final form 25 June 2020)

ABSTRACT

Within the tropical Pacific intertropical convergence zone (ITCZ), organized cloud systems that evolve over synoptic time scales frequently propagate eastward and contribute significantly to the clouds and precipitation in that region. This study analyzes eastward-propagating disturbances (EPDs) in the tropical Pacific during boreal winter (DJF) and spring (MAM) and their connection to Northern Hemisphere (NH) extratropical Rossby wave activity using cloud and precipitation fields from satellite and dynamical fields from reanalysis. During DJF, EPDs are located north of the ITCZ (around 15°N), propagate eastward at 10 m s^{-1} within the central Pacific, and exhibit high cloudiness associated with upper-level divergence on the east side of NH Rossby waves propagating into the tropics. During MAM, EPDs initiate in the west Pacific and propagate along the ITCZ axis (around 7°N) into the east Pacific at 15 m s^{-1} where NH Rossby waves induce upper-level divergence, enhancing their convective activity. The MAM EPDs are decidedly associated with Kelvin wave characteristics, while the DJF EPDs are not. The shallow meridional circulation (SMC) in the east Pacific is also studied in the context of EPDs. During DJF, EPDs do not impact the SMC, but the deep meridional circulation in the northern part of the ITCZ strengthens. During MAM, the shallow convection ahead of the EPDs enhances the SMC in the southern part of the ITCZ. These results distinguish between two types of EPDs during DJF and MAM that have different physical characteristics, forcing mechanisms, and regional impacts.

1. Introduction

Convection in the intertropical convergence zone (ITCZ) occurs on many time and space scales, from localized cells lasting an hour or less to widespread convective activity ebbing and flowing over many weeks. An important subset of this convective variability can be characterized as eastward-propagating disturbances (EPDs) occurring at synoptic time scales (i.e., on the order of a few days to two weeks) with eastward phase propagation. Kelvin waves can be considered one of the dominant synoptic-scale convective modes in the Pacific basin (Straub and Kiladis 2002; Roundy and Frank 2004; Huang and Huang 2011). The Kelvin wave is a solution of the shallow water equations on an equatorial beta plane (Matsuno 1966). Convectively coupled Kelvin waves propagate eastward along the ITCZ and arise from the interaction between dry Kelvin waves and moist convective processes (Straub and Kiladis 2003). Although Kelvin waves propagate at around 12–15 m s^{-1}, a particular phase speed itself is not proof that an EPD is a Kelvin wave. Rather, the large-scale kinematic and thermodynamic perturbations associated with an EPD should be consistent with the Kelvin wave solution from the shallow water equations (Kiladis et al. 2009).

Extratropical Rossby waves play a potentially important role in forcing tropical convection (e.g., Stan et al. 2017; Ortega et al. 2018). In relation to the Pacific basin, Straub and Kiladis (2003) reported that extratropical Rossby waves originating in the Southern Hemisphere (SH) can initiate Kelvin waves in the tropical west Pacific in boreal summer by inducing upper-tropospheric divergence and vertical motion as the Rossby waves propagate into the tropics. Liebmann et al. (2009) showed that some Kelvin waves over South America are initiated by SH extratropical Rossby waves in boreal winter. Kiladis and Weickmann (1992, 1997) and Kiladis (1998) found

Corresponding author: Lidia Huaman, lidiana.huaman@tamu.edu

DOI: 10.1175/MWR-D-20-0029.1

that NH extratropical Rossby waves enhance local cloudiness with eastward propagation in the vicinity of the central and east Pacific ITCZ during boreal winter; however, these disturbances did not appear to correspond to Kelvin waves.

The Kelvin wave signal in the tropical Pacific is at a minimum during boreal winter (Roundy and Frank 2004) and much stronger in boreal spring (Baranowski et al. 2016). The weaker Kelvin wave signal in DJF could be due to the intensification of the east Pacific cold tongue that inhibits convection around the equator along with the weak SH wave Rossby wave activity, limiting Kelvin wave initiation in the west Pacific. However, the relationship between NH extratropical Rossby waves and Kelvin waves (and eastward disturbances more generally) in the tropical Pacific remains understudied for boreal winter and is virtually unstudied for boreal spring.

The east Pacific is home to a shallow meridional circulation (SMC) in addition to the deeper Hadley cell associated with deep ITCZ convection (Trenberth et al. 2000; Zhang et al. 2004, 2008). The meridional overturning circulation in the east Pacific ITCZ is dominated by a shallow circulation in the southern part of the ITCZ and a deep circulation in the northern part of the ITCZ (Huaman and Takahashi 2016; Huaman and Schumacher 2018). The SMC exists year-round in the east Pacific, but is more dominant in DJF compared to MAM because of the existence of the double ITCZ north and south of the equator during boreal spring. The vertical structure of a Kelvin wave is tilted in the zonal direction, with maximum low-level convergence ahead of the Kelvin wave and maximum upper-tropospheric zonal divergence behind the location of low-level convergence (Kiladis et al. 2009). Straub and Kiladis (2002) reported that Kelvin wave propagation in the east Pacific evolves from shallow congestus clouds to organized deep convective features. Thus, there is a likelihood that the meridional overturning structure in the east Pacific may be altered during the passage of EPDs, including Kelvin waves.

This paper analyzes the characteristics and extratropical forcing of EPDs in the tropical Pacific during boreal winter (DJF) and spring (MAM), as well as associated variations in the meridional overturning circulation in the east Pacific. We utilize brightness temperature (T_b) for cloud properties, satellite precipitation for convective intensity, and reanalysis data for dynamical fields. We focus on DJF and MAM due to the strong NH wave activity during these seasons. This article is organized as follows: section 2 explains the data and methodology, section 3 describes the eastward disturbances in the tropical Pacific during DJF and MAM, followed by the meridional overturning circulation variations associated with these EPDs in section 4, and summary and conclusions are in section 5.

2. Data and methodology

We used daily T_b with a resolution of 0.5° × 0.5° from Cloud Archive User Services (CLAUS), which utilizes geostationary and polar-orbiting images (Hodges et al. 2000), for the period 1984–2016. Daily precipitation from the Tropical Rainfall Measuring Mission (TRMM) product 3B42 (Huffman et al. 2007) for the period 1998–2016 was also used to quantify precipitation. TRMM 3B42 data are available at 0.25° × 0.25° resolution and we regridded this data to 0.5° × 0.5° using bilinear interpolation. In addition, this study utilized daily wind, geopotential height, omega and temperature fields interpolated to a resolution of 2.5° × 2.5° from the Modern-Era Retrospective Analysis for Research and Applications V2 (MERRA2) reanalysis (Bosilovich et al. 2015) for the period 1984–2016 to characterize the atmospheric circulation associated with the EPDs and meridional overturning circulation. Huaman and Schumacher (2018) showed that MERRA2 better reproduces the east Pacific atmospheric conditions compared to other commonly used reanalyses, especially with respect to the complex vertical structure of convection observed by satellite.

Daily T_b anomalies were calculated by removing the first three harmonics, which represent the seasonal cycle. Frequency–wavenumber diagrams from Wheeler and Kiladis (1999) were then calculated for the central and east Pacific. This study is focused on high-frequency variability, so we used 64-day window segments overlapping by 13 days and tapered the data using a Hann window similar to Dias et al. (2013) to allow a smooth Kelvin signal distribution while excluding much of the intraseasonal signal associated with the Madden–Julian oscillation. From the frequency–wavenumber diagram, we retained the T_b signal with a period between 2.5 and 20 days and wavenumbers equal to and greater than +1 using Fourier filters (Figs. 1a,b). The result is called the eastward band T_b and includes the Kelvin-band signal.

The eastward band T_b was used to identify and characterize EPDs. Empirical orthogonal functions (EOFs) for DJF and MAM were used to isolate the maximum local eastward wave variance over the Pacific region from 15°S to 20°N and from 180° to 80°W (we slightly decreased the spatial domain to 150°–85°W, and similar results were obtained). In all cases the leading modes occur as pairs of EOFs, the combination of which represent eastward-propagating features. We regressed the

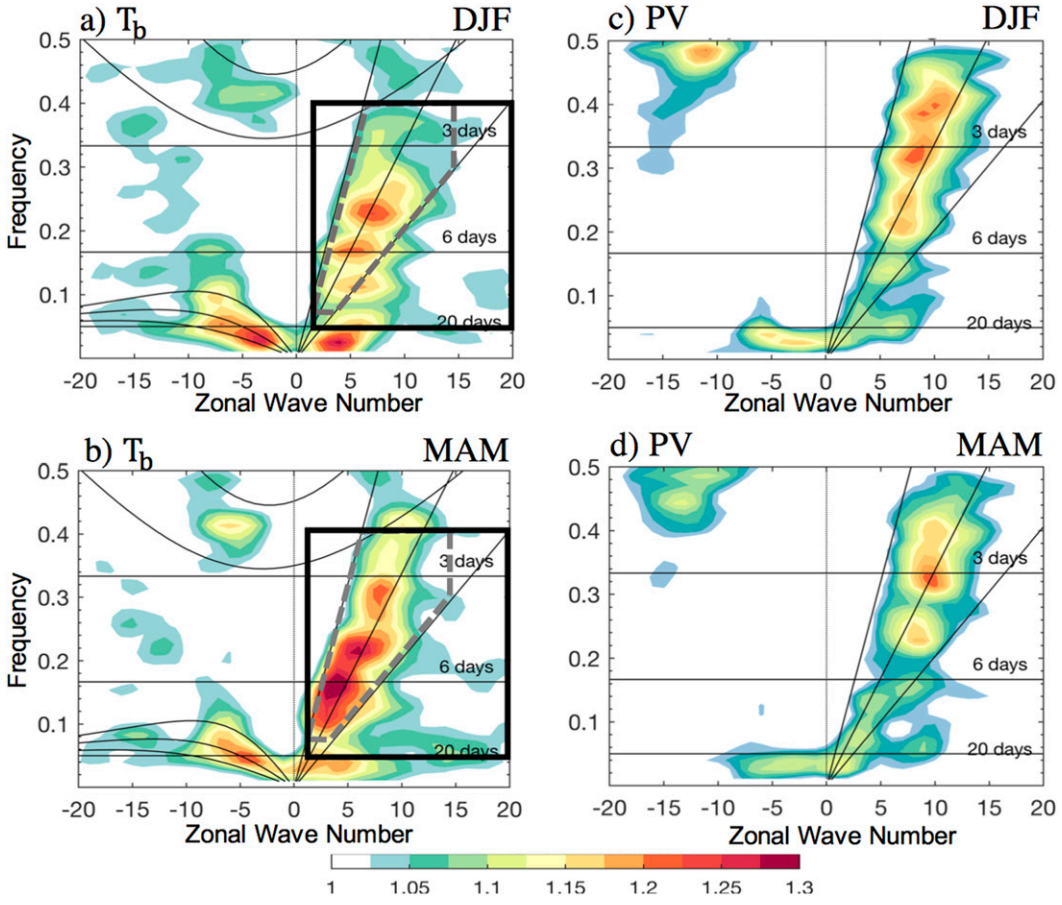

FIG. 1. Wavenumber–frequency power spectrum (from 120°E to 60°W) of the symmetric component of T_b summed from 15°S to 15°N for 1984–2016 for (a) DJF and (b) MAM. Thin black lines represent the dispersion curves for equivalent depths of 9, 25, and 90 m CCEWs. Heavy dashed gray and solid black boxes represent regions of Kelvin-band and east-band filtering, respectively. Wavenumber–frequency power spectrum (from 120°E to 60°W) of total 200-hPa PV summed from 20° to 50°N for (c) DJF and (d) MAM.

total dynamic fields against the first PC time series at different lags and levels for the two seasons to obtain the statistical behavior of each mode. A similar regression technique using a base point T_b instead of EOFs was also applied by Straub and Kiladis (2003) to characterize extratropical forcing of Kelvin waves by SH Rossby waves.

The linear regression results based on PC1 were scaled to a 12°C anomaly in T_b at the base point on day 0, a typical value for an eastward-propagating event. It is worth mentioning that the standard deviation of the filtered T_b is around 9.5°C at 130°W at the latitude of the ITCZ (7.5°N) during DJF and MAM. The statistical significance of these results was calculated based on a local two-sided significance test, which takes into account the correlation coefficients and a reduced number of degrees of freedom based on the decorrelation time scale (Livezey and Chen 1983). Results were considered significant at the 95% level or greater.

3. EPDs in the tropical Pacific

a. Mean state conditions

Figure 2 shows a Hovmöller diagram from December 2007 to May 2008 of the T_b anomaly from 2.5° to 12.5°N overlain by the eastward band T_b in black contours. EPDs are evident in both boreal winter (DJF) and spring (MAM) in the Pacific basin. During MAM, EPDs propagate from the west Pacific through the east Pacific at around 15 m s^{-1}, such as the event on 27 March (second star), consistent with Kelvin wave phase speeds and lifetimes (Straub and Kiladis 2002). Additional EPDs are shown during DJF that initiate in the central Pacific and have zonal phase speeds between 10 to

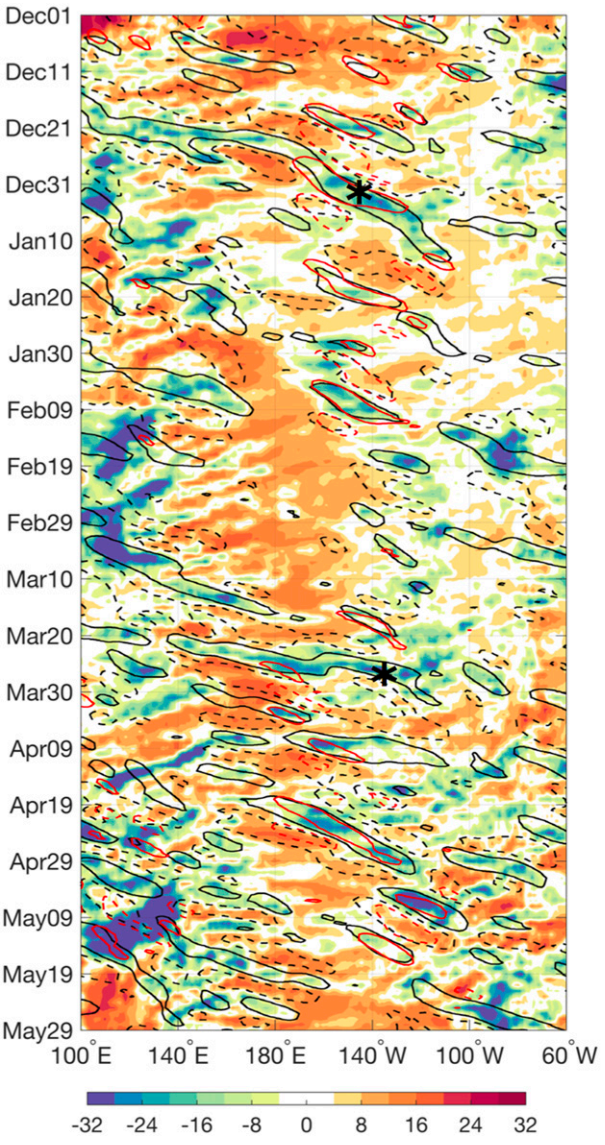

FIG. 2. Hovmöller diagram of T_b anomalies (shaded) and eastward 2.5–20-day band T_b in °C along 2.5°–12.5°N (black contours; 4°C solid, −4°C dashed) and 10°–20°N (red contours; 8°C solid, −8°C dashed) from December 2007 to May 2008. The stars show two EPD events on 1 Jan and 27 Mar.

$13\,m\,s^{-1}$, such as the event on 1 January (first star). These waves are slower and more longitudinally confined than the MAM waves, which suggests that they may be different phenomena. The Hovmöller diagram between 10° and 20°N (red contours in Fig. 2) indicates that these DJF events are stronger north of the ITCZ, but are still initiated in the central Pacific and retain the same zonal phase speed.

The left panels in Fig. 1 show the climatological wavenumber–frequency power spectrum of T_b across the tropical Pacific (from 120°E to 60°W and from 15°S to 15°N) for DJF and MAM. Both seasons exhibit significant power in the eastward band T_b region (solid box), consistent with Fig. 2. However, the Kelvin wave signal (dashed region) is weaker in DJF compared to MAM.

The right panels in Fig. 1 show the climatological wavenumber–frequency diagram of PV at 200 hPa in the extratropical Pacific (from 120°E to 60°W and from 20° to 50°N) for DJF and MAM. Extratropical Rossby wave activity is well represented by PV, which is approximately conserved (Bluestein 1992) and frequently propagates into the tropics over the central and eastern Pacific (Kiladis and Weickmann 1992, 1997; Tomas and Webster 1994; Kiladis 1998). While Kelvin waves are equatorially trapped and cannot be present at this latitude range, a strong eastward PV signal in the 2.5–20-day band is evident during both seasons, with power concentrated at higher zonal wavenumbers than in Kelvin waves. Thus, Figs. 1c and 1d show that Rossby waves propagate eastward in the NH extratropics with a similar phase speed as Kelvin waves. This strong signal is also seen in the wavenumber–frequency diagram of meridional wind and at a range of latitudes bands extending from the extratropics into the tropics (not shown). Pena-Ortiz et al. (2013) showed that the 200-hPa wind field north of the equator in the central and east Pacific is dominated by a subtropical jet, which is stronger during DJF than MAM. Figures 1c and 1d show that the PV signal at the latitudes of the subtropical jet is also slightly stronger during DJF compared to MAM. Figure 3 further compares each season's background circulation and precipitation and cold cloud field.

The left panels of Fig. 3 show the geographical distribution of the eastward band T_b and precipitation variance over the tropical Pacific for DJF and MAM. To focus on the tropical distribution of T_b and precipitation, we masked out values poleward of 20°N. The 30-day high-pass-filtered **E**-vectors at 200 hPa (Hoskins et al. 1983) are also plotted. The **E**-vector is calculated as $\overline{v'^2 - u'^2}$, $-\overline{u'v'}$, where u and v are the zonal and meridional wind, respectively. The primes represent 30-day high-pass fluctuations and the bars represent seasonal averages. **E**-vectors provide a qualitative measure of the amplitude and direction of propagation of upper-tropospheric extratropical wave activity and point in the approximate direction of the group velocity of a wave packet (Hoskins et al. 1983; Kiladis 1998; Straub and Kiladis 2003).

In the North Pacific during DJF (Fig. 3a), the **E**-vectors point southeastward indicating that the preferred path of extratropical Rossby wave energy is equatorward into the central and eastern tropical Pacific. The eastward band T_b variance (from 1984 to 2016) shows lower

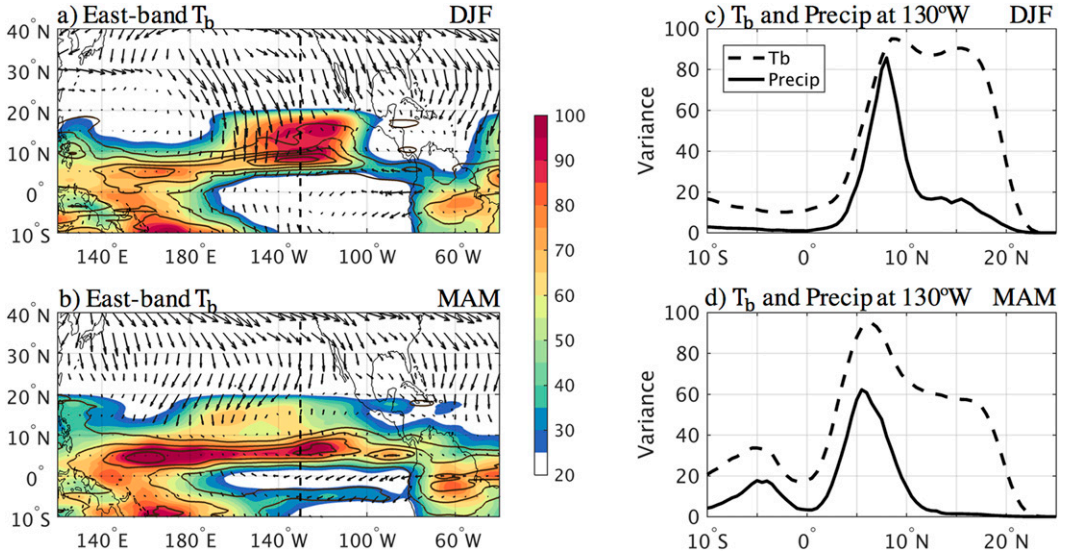

FIG. 3. Climatological eastward 2.5–20-day band T_b (1984–2016, shaded) and precipitation (1998–2016, contours) variance in $°C^2$ and $mm^2\,day^{-2}$, respectively, and 30-day high-pass-filtered **E**-vectors (1984–2016) in $m^2\,s^{-2}$ for (a) DJF and (b) MAM. Precipitation contour interval is $15\,mm^2\,day^{-2}$, T_b values poleward of 20°N are masked out. Meridional cross sections at 130°W of T_b and precipitation variance for (c) DJF and (d) MAM.

values in the west Pacific and two relative maxima in the east Pacific at 7.5° and 17°N. While the eastward band precipitation variance (from 1998 to 2016) also shows lower values in the west Pacific, there is only one peak in the east Pacific at 7.5°N. This structure is similar when considering the same time range (from 1998 to 2016) for T_b and TRMM rainfall (not shown). Figure 3c shows a meridional cross section of the variance of the eastward band precipitation and T_b at 130°W. Precipitation variance is large in the ITCZ at 7.5°N, but drops off rapidly on either side of the ITCZ. The T_b variance also peaks at 7.5°N, but remains large until its second peak at 17°N. Figures 3a and 3c suggest that extratropical perturbations modulate high-cloud structure (and to a lesser extent rainfall) north of the ITCZ up to 20°N during DJF. This result is consistent with Kiladis (1998), who proposed that the intrusion of positive PV associated with extratropical Rossby wave perturbations into low latitudes modulates cloudiness and vertical motion in the vicinity of the ITCZ during DJF.

During MAM (Fig. 3b), a large eastward band T_b and precipitation signal exists in the west Pacific and may be mostly accounted for by the Kelvin band (Fig. 1b). Eastward band T_b and precipitation variance remains strong north of the equator as Kelvin waves propagate eastward from the west Pacific into the east Pacific. A much weaker secondary maximum occurs south of the equator, extending the southern ITCZ over the easternmost Pacific. The meridional precipitation variance cross section at 130°W (Fig. 3d) shows a double ITCZ at 5°S and 7.5°N. The double ITCZ is also evident in the eastward band T_b, and while there is some T_b variance poleward of the northern branch of the ITCZ, the signal is not as strong as in DJF (Fig. 3c). The **E**-vectors in the North Pacific during MAM (Fig. 3b) point mainly southwestward, indicating that Rossby wave perturbations in the subtropical jet tend to propagate equatorward into the west and central tropical Pacific.

b. Horizontal structure of eastward 2.5–20-day band regressions

To examine the horizontal structure of EPDs in the Pacific region, we used EOFs of eastward band T_b to isolate the leading modes of EPDs over the central and east Pacific (15°S–20°N, 180°–80°W). Figure 4a shows the contribution of the first four EOFs for DJF and MAM. The leading EOF pairs explain 15.4% and 11.2% in DJF and MAM, respectively. Additionally, the cross correlation between PC1 and PC2 reach up to +0.8 at day +1, and −0.8 at day −1. Because the results based on EOF1 are similar to those based on EOF2, we will focus on the leading EOF in the remainder of this study.

During DJF (Fig. 4b), EOF1 suggests an eastward wave that propagates at 15°N with a local zonal wavenumber of about 7. When PC1 values are positive, minima in T_b suggest wet conditions and maxima in T_b suggest dry conditions. Thus, wet conditions are observed at 140°W and dry conditions are observed at 115°W. When PC1 values are negative, conditions are opposite, and it is dry at 140°W and wet at 115°W. This EPD

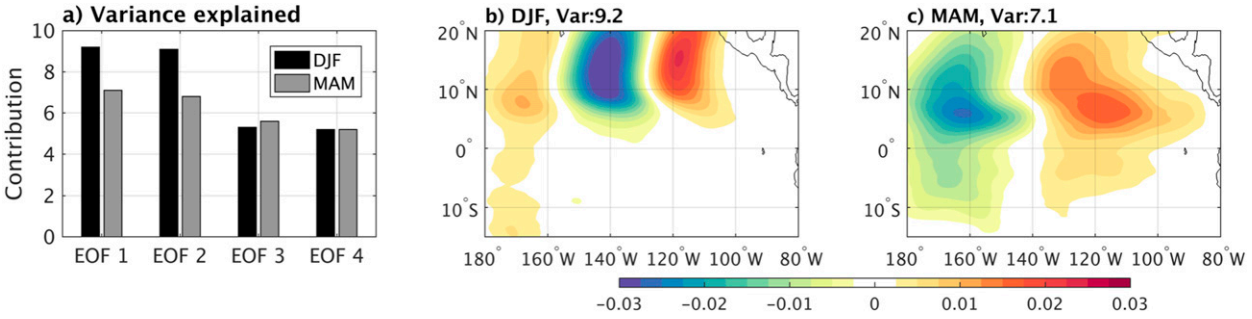

FIG. 4. (a) Contribution of variance explained by the first four EOFs for both seasons. First EOF of eastward 2.5–20-day band T_b for (b) DJF and (c) MAM.

propagates zonally well to the north of the main axis of the ITCZ through the strongest region of extratropical Rossby wave activity (Fig. 3a). During MAM (Fig. 4c), the EPD suggested by EOF1 propagates at 7.5°N, which is along the climatological ITCZ axis, and has a local zonal wavenumber of around 4. Wet (dry) conditions are observed at 160°W (120°W). The T_b signal extends across the equator and shows an enhanced secondary signal around 5°S consistent with the double ITCZ structure during boreal spring.

To characterize the large-scale atmospheric circulation associated with EPDs, the total T_b, precipitation, winds, geopotential height, and streamfunction fields are regressed onto PC1. Figure 5 shows the regressed structure during DJF at 850 and 200 hPa at different lag days. At day −4 (Fig. 5a), a positive T_b perturbation is seen at 140°W with a weak negative T_b perturbation at 160°W. The negative T_b perturbation propagates along 15°N to 155°W at day −2 and to 140°W at day 0 (Figs. 5b,c), consistent with Fig. 4b. The 850-hPa geopotential height and wind signal is weak over the equatorial region with values under 10 m and 2 m s^{-1}, respectively. At 200 hPa (Figs. 5e–h), a Rossby wave train is seen in the central Pacific propagating southeastward. The negative T_b signal is associated with the southwesterly flow ahead of the Rossby wave trough, consistent with Fig. 3a. This interaction was well documented in Kiladis and Weickmann (1992) and Kiladis (1998). A comparison between T_b in shading and precipitation (for the period 1998–2016) in thick contours shows that, while the rainfall signal is concentrated within the ITCZ, the T_b signal with its center farther north is primarily associated with high cloudiness. The divergence at 200 hPa at day 0 is shown in Fig. 7a and the high cloudiness is associated with the positive upper-level divergence and southerly winds on the trough side of the Rossby wave. This structure is also seen at other lags (not shown).

A more complex structure associated with EPDs is seen during MAM (Fig. 6). At day −4 (Figs. 6a,e), a negative T_b signal is located close to the equator in the west Pacific but is then displaced off the equator as it propagates eastward along the ITCZ axis at 7.5°N at later lag days. At day −2 (Fig. 6b), the 850-hPa geopotential height field has a center at the equator with positive anomalies up to 20 m, with a primarily zonal wind field in phase with the geopotential as in a theoretical Kelvin wave (Matsuno 1966). Dynamical fields centered on the equator accompanied by off equatorial convective signals are also seen for convectively coupled Kelvin waves during JJA (Straub and Kiladis 2002, 2003). At day 0 (Fig. 6c), the 850-hPa winds suggest convergence around 145°W, ahead of the strongest negative T_b signal at 160°W. This structure is consistent with the description of Kelvin waves in Kiladis et al. (2009).

Figure 6 also indicates enhancement of negative T_b at 15°N, similar to the EPDs observed during DJF. As in DJF, a comparison with TRMM precipitation (in contours) shows that this T_b enhancement is primarily associated with nonprecipitating high cloudiness and at 200 hPa (Figs. 6e–h), a Rossby wave train appears to modulate the negative eastward T_b perturbations at 15°N. However, the Kelvin wave at 7.5°N and EPD at 15°N occur at the same longitudes during MAM and can potentially interact. This extratropical–tropical connection is most clear at days −2 and 0 (Figs. 6f,g), when the upper-level cyclonic circulation on the trough side of the Rossby wave interacts with the upper-level equatorial westerly winds between the convective and nonconvective part of the Kelvin wave around 160°W. This pattern also induces strong upper-level divergence in the Kelvin wave at 7.5°N at day 0 (Fig. 7b). At day +2, the Kelvin wave modulates precipitation in the double ITCZ at 5°S and 5°N (Fig. 6d).

To synthesize the propagation characteristics of eastward disturbances and their associated extratropical forcing during DJF and MAM, Fig. 8 shows the time–longitude diagram of regressed T_b and 200-hPa streamfunction from

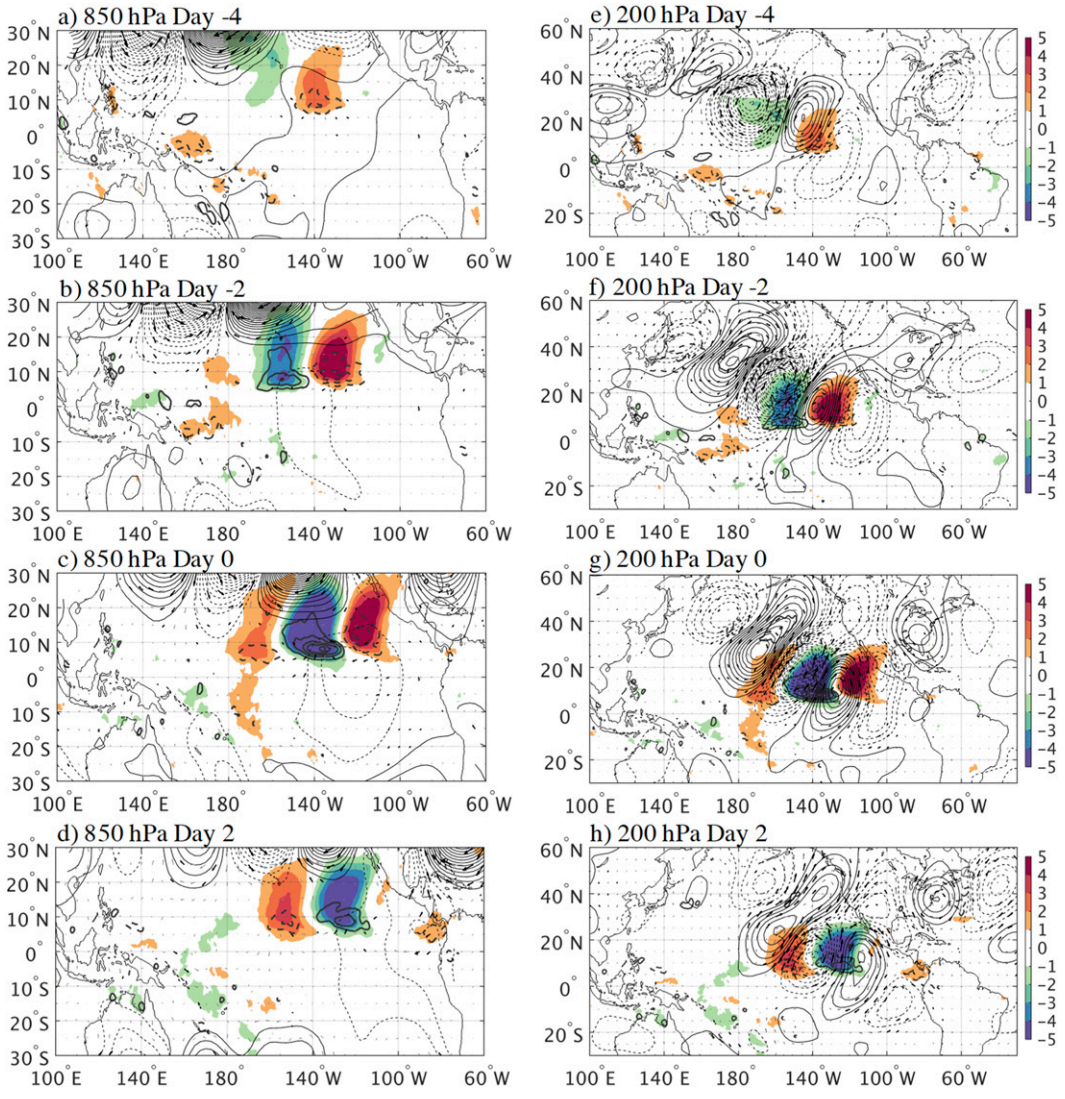

FIG. 5. Regressed values of (a)–(d) T_b in °C (shading), geopotential height in m (contours), precipitation in mm day^{-1} (thick contours), and winds (vectors) at 850 hPa, and (e)–(h) streamfunction in m^2 s^{-1} (contours) and winds (vectors) at 200 hPa, based on PC1 at different lags during DJF. Panels (e)–(h) are on a different spatial scale than (a)–(d). Geopotential height (streamfunction) contour interval is 4 m (2×10^5 m^2 s^{-1}), precipitation contour interval is 1 mm day^{-1}. Locally significant winds are shown in bold vectors, with the largest vector around 3 m s^{-1}. The shading in (e)–(h) is as in (a)–(d).

2.5° to 12.5°N for both seasons. During DJF (Fig. 8a), the eastward wave covers less longitudinal extent than MAM and a positive (negative) 200-hPa streamfunction perturbation is located ahead (behind) of the minimum T_b, consistent with Fig. 5 and the forcing of slower moving EPDs from the extratropics. The NH Rossby wave propagation estimated from the 200-hPa streamfunction has a similar phase speed (10 m s^{-1}). During MAM (Fig. 8b), the T_b signal propagates eastward at 15 m s^{-1}, consistent with a Kelvin wave; however, the NH Rossby wave estimated from the 200-hPa streamfunction still propagates at 10 m s^{-1} and the streamfunction signal does not precede the T_b minimum as in DJF. This indicates that while extratropical Rossby waves may not initiate Kelvin waves, they may strengthen their convective signal by causing upper-level divergence in the preexisting Kelvin wave (Fig. 7b).

To see if our regression-based results are consistent with the occurrence and evolution of individual Kelvin events, we identified 42 case studies of EPDs (i.e., eastward 2.5–20-day T_b larger than 1.25 standard deviation) that propagate at 15 m s^{-1} from the west Pacific to

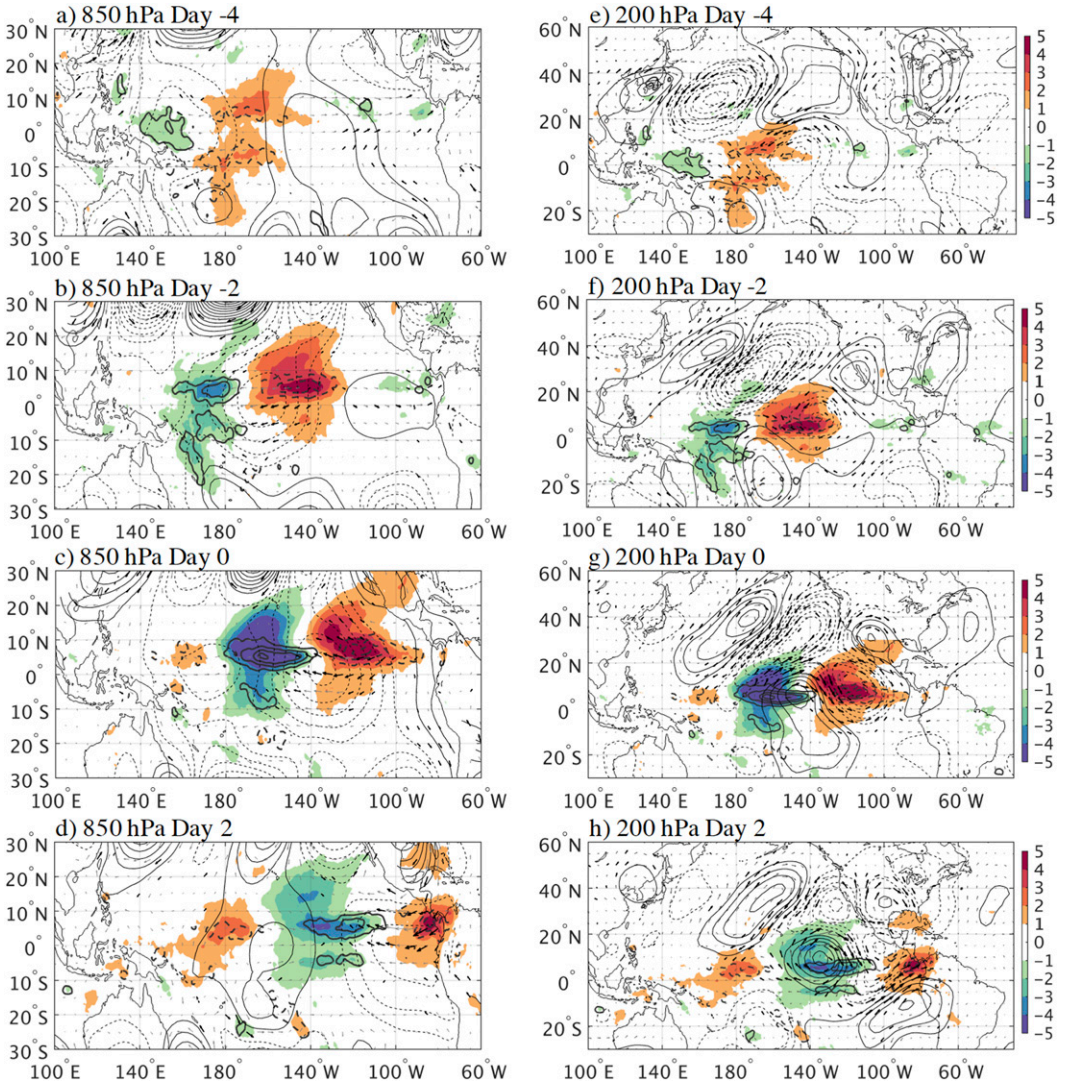

FIG. 6. As in Fig. 5, but for MAM.

east Pacific for at least five days in MAM in the east Pacific from 1984 to 2016. While ten of these EPDs propagated across the tropics without interacting with NH extratropical Rossby waves, 32 were associated with extratropical forcing (i.e., negative geopotential height anomaly intrusion into the tropics on the trough side of the extratropical Rossby wave). Eleven of these 32 EPDs were excited from NH extratropical Rossby waves in the central Pacific, similar to what we postulate happens in DJF. These EPDs were sometimes as fast as Kelvin waves. However, the other 21 EPDs were Kelvin waves that initiated in the Indian Ocean, Maritime Continent, or west Pacific. As these Kelvin waves moved eastward, they interacted with an extratropical Rossby wave in the central and east tropical Pacific. It is worth mentioning that most of the ten EPDs that do not interact with the NH extratropical Rossby waves seem to be initiated or strengthen by the SH extratropical Rossby waves in the west and central Pacific as suggested by Straub and Kiladis (2003).

c. *Vertical structure of eastward 2.5–20-day band regressions*

In this section, we examine the vertical structure of the EPDs in DJF and MAM. The time–height cross section of zonal wind anomalies from the equator to 10°N at 140°W for DJF is shown in Fig. 9a. At 200 hPa, the zonal wind anomalies reflect the Rossby wave train, such that the anomalous westerlies at day 0 correspond to the wave trough, which also supports the northerly flow seen in Fig. 5g. Similarly, the upper-level anomalous easterly flow at day −5 corresponds to the Rossby

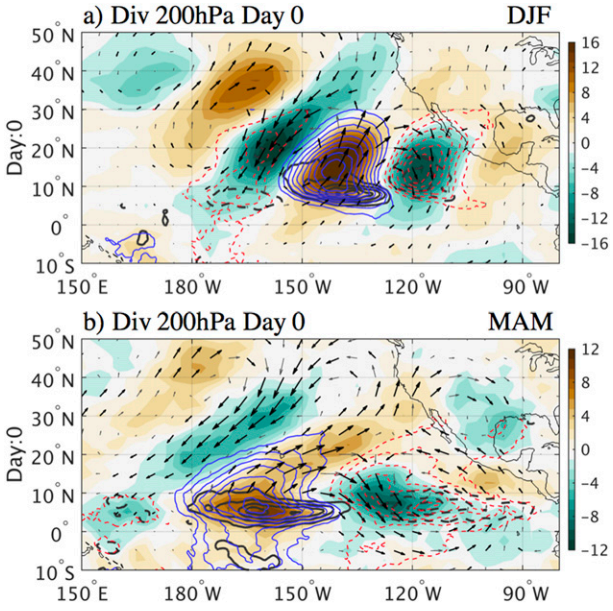

FIG. 7. Regressed values of T_b in °C (contours), 200-hPa divergence in 10^{-6} s^{-1} (shaded), and winds in m s^{-1} (vectors) at lag day 0 for (a) DJF and (b) MAM; T_b contour interval is 1°C. Locally significant winds are shown in bold vectors, with the largest vector around 3 m s^{-1}.

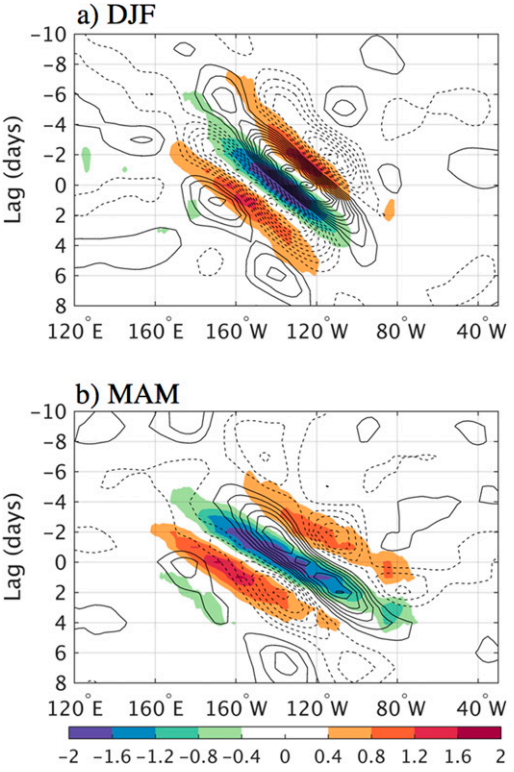

FIG. 8. Longitude–time diagram of regressed T_b in °C (shading) and 200-hPa streamfunction in m^2 s^{-1} (contours), averaged from 2.5° to 12.5°N from day −10 to day 8. Contour interval is 1×10^5 m^2 s^{-1} with positive (negative) values in solid (dashed) contours.

wave ridge (Fig. 5e). The time–height structure is tilted; negative values of zonal wind anomalies are seen at higher levels on day −5 and transition to lower levels on day 0. So one would experience anomalous easterly winds at upper levels before the wave passage and anomalous low-level easterlies as the wave passes. A similar tilt is seen in positive zonal wind anomalies after the passage of the EPD such that there are anomalous westerly winds aloft when the wave passes that then work their way down to the mid troposphere on day +5. The time axis in this cross section can also be viewed as a longitude–height cross section of the EPD. Therefore, the structure in Fig. 9a is tilted upward and eastward with height. The zonal wind anomaly cross section for MAM at 160°W (Fig. 9b) tilts westward with height and corresponds closely to a Kelvin wave structure, with low-level convergence and upper-level divergence around day 0 (Straub and Kiladis 2002; Kiladis et al. 2009). The upper-level anomalous westerly flow at day −2 is strengthened as a result of the interaction of the Kelvin wave and trough of the extratropical Rossby wave. Thus, the zonal wind vertical structure of the two types of eastward disturbances further differentiate them from one another.

NH extratropical Rossby wave propagation into the tropics is associated with the intrusion of high PV into low latitudes (Kiladis and Weickmann 1992; Tomas and Webster 1994). The left panels of Fig. 10 show 200-hPa PV at different lag days during DJF overlain by 200-hPa wind vectors and T_b and TRMM precipitation contours, while the right panels show the meridional circulation at 140°W for each lag day. At day −3 (Fig. 10a), the minimum T_b is at 160°W and is located east of the Rossby wave trough (i.e., positive PV) with upper-tropospheric southerly flow. It is interesting to note that the Rossby wave trough is tilted southwest–northeast, therefore the T_b is also tilted in this direction, especially at later lag days. At 140°W, positive T_b occurs with negative PV and peaks at 12.5°N. Descending motions predominate (Fig. 10d), while weak ascending motion at 25°N is associated with the tilted Rossby wave trough and upper-level divergence (not shown). As the EPD progresses eastward from day −3 to day −1, the minimum T_b shifts to 145°W (Fig. 10b). While the rainfall signal is concentrated within the ITCZ, the T_b signal with its center farther north is primarily associated with high cloudiness. Strong ascending motion in the mid- to upper troposphere is seen between 15° and 25°N in the 140°W cross section (Fig. 10e), along with a strong southerly

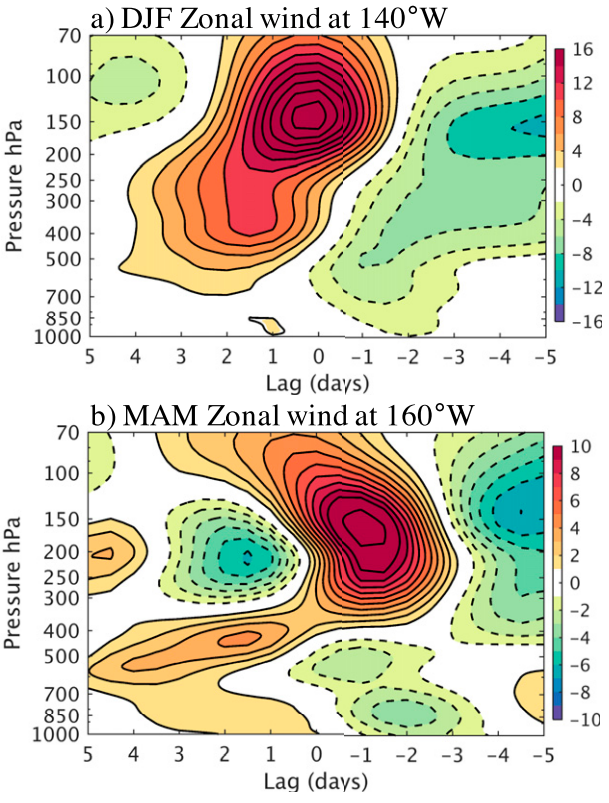

FIG. 9. Time–height cross sections of zonal wind anomalies in m s^{-1} from the equator to 10°N for (a) DJF at 140°N and (b) MAM at 160°N.

flow associated with the Rossby wave trough. Ascending motion is relatively weak at low levels. This region is dominated by midlevel convergence and lower and upper-level divergence (not shown), which is consistent with a stratiform rain structure (Mapes and Houze 1995).

At day 0 (Fig. 10c), the EPD has a negative T_b peak at 140°W and propagates along 15°N, several degrees north of the climatological ITCZ where the regressed TRMM precipitation signal maximizes (i.e., at 7.5°N). The positive PV advection associated with the trough side of the extratropical Rossby wave enhances upward motion throughout the troposphere in the vicinity of the climatological ITCZ and to its north (Fig. 10f), although the maximum upward motion is still confined to upper levels and this drives the cloudiness signal as reflected in the T_b field. This analysis shows that the midlevel forcing from the NH Rossby wave trough enhances ITCZ precipitation and suggests that the convection in the ITCZ evolves from shallow to deep during the passage of EPDs during DJF.

Figure 11 shows a similar set of plots for MAM, with the vertical cross section taken at 160°W. At day −3 (Fig. 11a), the convectively active part of the Kelvin wave is centered at 160°E along the equator and appears removed from the influence of the extratropical Rossby wave. A northeastward tilting upper-level cloud signal centered at 25°N, 170°W is being initiated/modulated by the NH Rossby wave ahead of the Kelvin wave. At 160°W, the convectively suppressed part of the Kelvin wave peaks at 5°N, where descending motion is observed in the mid- to upper troposphere (Fig. 11d). By day −1 (Fig. 11b), the Kelvin wave has propagated along the ITCZ axis and has caught up with the upper cloud signal from farther north. This EPD is positively tilted within the Rossby wave structure, as in DJF. Figure 11e shows the vertical structure of the Kelvin wave ahead of the T_b minimum. Low- to midlevel upward motion is observed ahead of the Kelvin wave with a peak at 800 hPa, consistent with the fact that the convective cloud population progress from shallow to deep as a Kelvin wave propagates eastward over a particular location (Straub and Kiladis 2002). This upward motion profile is in contrast to the DJF profile, which peaks in the mid- to upper troposphere (Figs. 10e,f). The omega field in Fig. 11e tilts upward and poleward with height, so that the EPD has peak ascending motion around 500 hPa at 17.5°N. Thus, while the Kelvin wave shows low-level convergence, the slower moving EPD vertical motion structure suggests low-level divergence. At day 0 (Fig. 11c), the T_b minimum associated with the Kelvin wave is located at 5°N, 160°W where the maximum upward motion peaks at 400 hPa (Fig. 11f), consistent with the deepening of convection during a Kelvin wave passage.

4. EPD impacts on the meridional overturning circulation

The east Pacific ITCZ has a two-mode vertical structure of convection: shallow and deep. Using reanalysis data, Back and Bretherton (2006) suggested a predominantly bottom-heavy vertical motion profile (i.e., shallow convection), with a maximum at 850 hPa controlled by a SMC and moist static energy import. However, satellite data suggest a top-heavy vertical motion profile, with a maximum at 400 hPa mainly from deep convective and stratiform rainfall (Schumacher et al. 2004; Hagos and Zhang 2010). Huaman and Schumacher (2018) studied the vertical structure of latent heating in the east Pacific ITCZ, which is closely related to vertical velocity, using TRMM and *CloudSat* data. They showed two peaks of latent heating at 850 and 400 hPa associated with shallow and deep convection, respectively. Shallow convection predominates in the southern part of the ITCZ where the meridional sea surface temperature (SST) gradient induces low-level convergence, and deep convection predominates in the northern part of

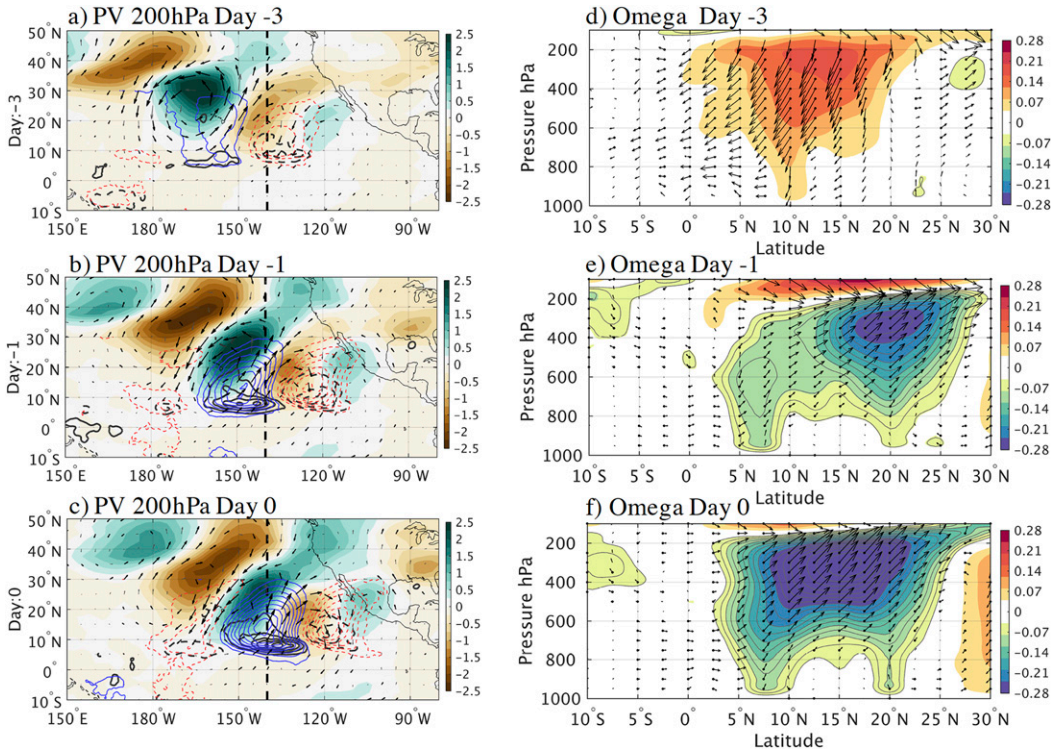

FIG. 10. Regressed values of (a)–(c) T_b in °C (blue and red contours), TRMM precipitation in mm day^{-1} (gray contours), potential vorticity in PV units (10^{-6} m^2 s^{-1} K kg^{-1}, shaded), and winds in m s^{-1} (vectors) at 850 hPa, and (d)–(f) pressure–latitude cross section across 140°W [dashed black lines in (a)–(c)] of omega in Pa s^{-1} and meridional flow (vertical velocity is amplified 15 times for better illustration), based on PC1 at different lags during DJF. T_b contour interval is 1°C. Locally significant winds are shown in bold vectors, with the largest vector around 3 m s^{-1}.

the ITCZ over the warm SST. This section will describe changes to the overturning meridional circulation and convective clouds in the east Pacific during the passage of slower moving EPDs confined to the central Pacific in DJF and faster moving Kelvin waves in MAM.

Zhang et al. (2008) identified the SMC in the east Pacific with the following criteria: (i) meridional wind at 700 hPa in the opposite direction of the near-surface wind and (ii) meridional wind either decreasing in magnitude or changing direction between 700 and 400 hPa. Using these criteria, the SMC is evident in the far east Pacific (140°–85°W) in DJF (Fig. 12a) and MAM (Fig. 12b), where the southerly component of the trade winds overturns at 800 hPa. In addition, there is a progressive transition from southerly to northerly winds in the central Pacific at 200 hPa during both seasons, which is associated with an upper-level trough in the South Pacific (Vincent 1994).

The vertical structure of omega and meridional flow along 120°W is shown in Figs. 12c and 12d for DJF and MAM, respectively. During DJF (Fig. 12c), upward motion is strongest at low levels in the ITCZ axis and is associated with a strong shallow meridional overturning. The weaker upper-level ascending motion around 15°N is related to the intrusion of NH Rossby waves with northerly flow that modulate cloudiness north of the ITCZ (Kiladis 1998). During MAM (Fig. 12d), upward motion in the ITCZ deepens, suggesting convection of greater vertical extent, and the shallow meridional overturning is less distinct (although still present as shown in Fig. 12b). The upper-level ascending motion around 15°N has weakened compared to DJF, but still may reflect the influence of NH Rossby waves over the central and east Pacific ITCZ. The double ITCZ is also apparent in Fig. 12d with the second ITCZ branch at 5°S shown by weak ascending motion below 750 hPa.

Figure 13 shows the vertical structure of omega and meridional circulation anomalies in the far east Pacific (120°W) during suppressed convection conditions, the transition from suppressed to deep convection, and deep convective conditions associated with EPDs during DJF and MAM. During both seasons, shallow (deep) vertical motion associated with suppressed (active) convection is

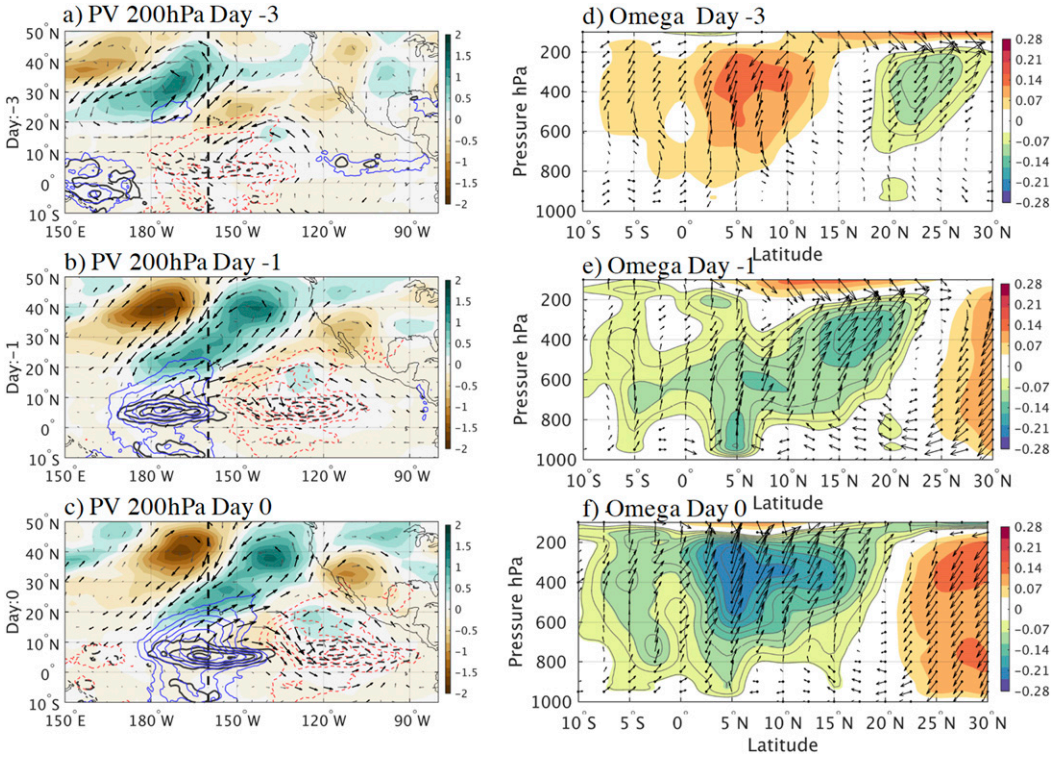

FIG. 11. As in Fig. 10, but for MAM. Cross sections (d)–(f) are at 160°W.

seen within the ITCZ at day 0 (+2), and the transition between these conditions occurs at day +1.

During DJF, EPDs are the result of extratropical Rossby waves propagating into the tropics and the meridional circulation north of the ITCZ is highly impacted, especially at mid- to upper levels (Figs. 13a–c). During suppressed convective conditions, northerly winds at 200 hPa associated with the NH Rossby wave ridge are associated with upper-level convergence, which produces descending motion in the ITCZ and to the north (Fig. 13a). Weak northerly flow at 700 hPa occurs near the top of the omega anomaly in the ITCZ and indicates a small contribution to the shallow meridional overturning south of the ITCZ. During the transition between suppressed and deep convection at day +1 (Fig. 13b), the extratropical Rossby wave trough and southerly winds at 200 hPa start inducing upper-level divergence and indirectly driving low-level convergence in the ITCZ (i.e., intensification of the trade winds), but little change in flow occurs at 700 hPa. At day +2 (Fig. 13c), strong upper-level vertical motion is observed in the ITCZ (around 7.5°N) and to the north and is associated with the upper-tropospheric southerly winds and enhanced divergence. Anomalous winds are southerly at 700 hPa, acting against the shallow meridional overturning. Therefore, while EPDs during DJF seem to strengthen the meridional circulation in the northern part of the ITCZ, the SMC south of the ITCZ is much less impacted. It is worth mentioning that the climatological ITCZ in the east Pacific during DJF has a bottom-heavy vertical motion structure with a maximum at 850 hPa (Huaman and Schumacher 2018). However, during the passage of EPDs, the vertical motion of the ITCZ evolves from bottom to top heavy as shown in Figs. 13a–c. Thus, EPDs can make the climatological vertical motion profile less bottom heavy during DJF.

During the passage of Kelvin waves in MAM, the meridional circulation in the far east Pacific is quite different than in DJF. At day 0 (Fig. 13d), suppressed convection is seen in the ITCZ region at 5°N and low-level divergence weakens the southerly and northerly trade winds. At 25°N, the tilted trough side of the extratropical Rossby wave (see Fig. 6g) produces ascending motion. On day +1 (Fig. 13e), the Kelvin wave propagates eastward over the far east Pacific and the shallow cloud population that precedes the deep convection in the Kelvin wave appears to strengthen the shallow meridional overturning in the southern part of the ITCZ (around 5°N). The strength of the SMC is consistent when we consider a smaller EOF domain that brackets the Kelvin wave in the far east Pacific (not shown). The SMC turns into a deep circulation at day +2

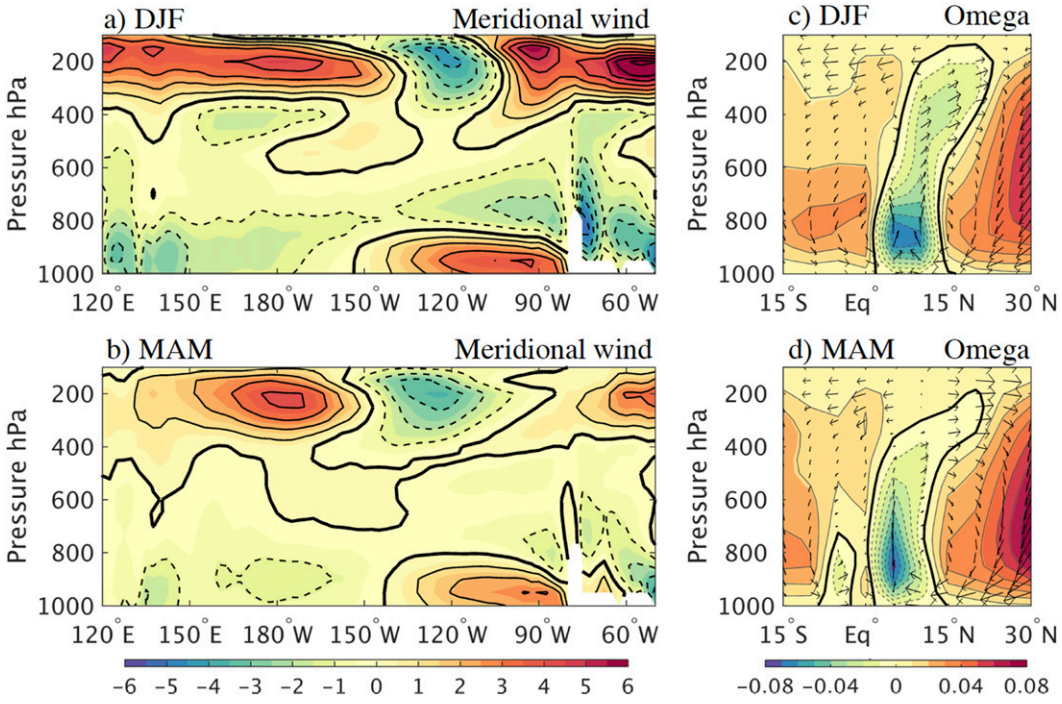

FIG. 12. Pressure–longitude cross section of the climatological (1984–2016) meridional wind in m s^{-1} at the equator for (a) DJF and (b) MAM. The zero wind line is marked by the heavy black contour. Meridional circulation over the east Pacific at 120°W in vectors (vertical pressure velocity is amplified 15 times for better illustration) and vertical pressure velocity (Pa s^{-1}, shaded) for (c) DJF and (d) MAM.

(Fig. 13f) when deep convection is observed over the east Pacific ITCZ. In addition, the passage of the Kelvin wave seems to alter the southern branch of the double ITCZ at 2.5°S, which evolves from shallow to deep convection. Thus, the southern branch of the ITCZ could be forced by both the extratropical Rossby and Kelvin waves, with both inducing upper-level divergence and low-level convergence, respectively. The meridional circulation in the northern part of the ITCZ does not seem be altered during Kelvin wave passages during MAM.

It has been shown that the vertical structure of vertical velocity and diabatic heating from reanalyses are inconsistent with one another and with satellite retrievals in the east Pacific due to the lack of observational constraints and limitations in the parent model convective parameterizations (e.g., Hagos and Zhang 2010). Therefore, we use measurements from the *CloudSat* profiling cloud radar, product 2B-GEOPROF (Stephens et al. 2002; Marchand et al. 2008), to see if there are different observed cloud structures associated with EPDs between seasons. We selected two case studies, a slow-moving EPD from 1 January 2008 and a Kelvin wave from 27 March 2008 (see Fig. 2). Figure 14 shows the upper-level dynamical field and cloud and precipitation structures along with vertical cross sections of *CloudSat* reflectivity for each event at 1000 and 2100 UTC, respectively.

During the slow-moving EPD (Figs. 14a,c), the ITCZ is between 10° and 16°N where there is a maximum in TRMM rainfall and deep convection observed by *CloudSat*. The EPD, which was initiated on the trough side of the extratropical Rossby wave, is located north of the ITCZ (around 17°–25°N) along with *CloudSat*-observed deep upper-level cloud but little rain at the surface, consistent with the DJF eastward band T_b and precipitation latitudinal distribution (Figs. 3a,c) and anomalies of vertical velocity in MERRA2 (Figs. 10f and 13c). South of the ITCZ, most of the observed clouds have very low tops (2 km or less).

During the Kelvin wave passage (Figs. 14b,d), the main ITCZ is between 5° and 10°N based on the TRMM rainfall and *CloudSat* cross section. The convection around 5°N appears to be evolving from congestus to deep convection rapidly based on the *CloudSat* reflectivity structure. Very little upper-level cloud is evident north of the ITCZ, which is also consistent with Figs. 3b and 3d. This Kelvin wave was forced by an extratropical Rossby wave and although the Rossby wave structure is not tilted as in Fig. 6g, the extratropical forcing mechanism seems to be similar. The trough side of the Rossby wave propagated into the tropics and

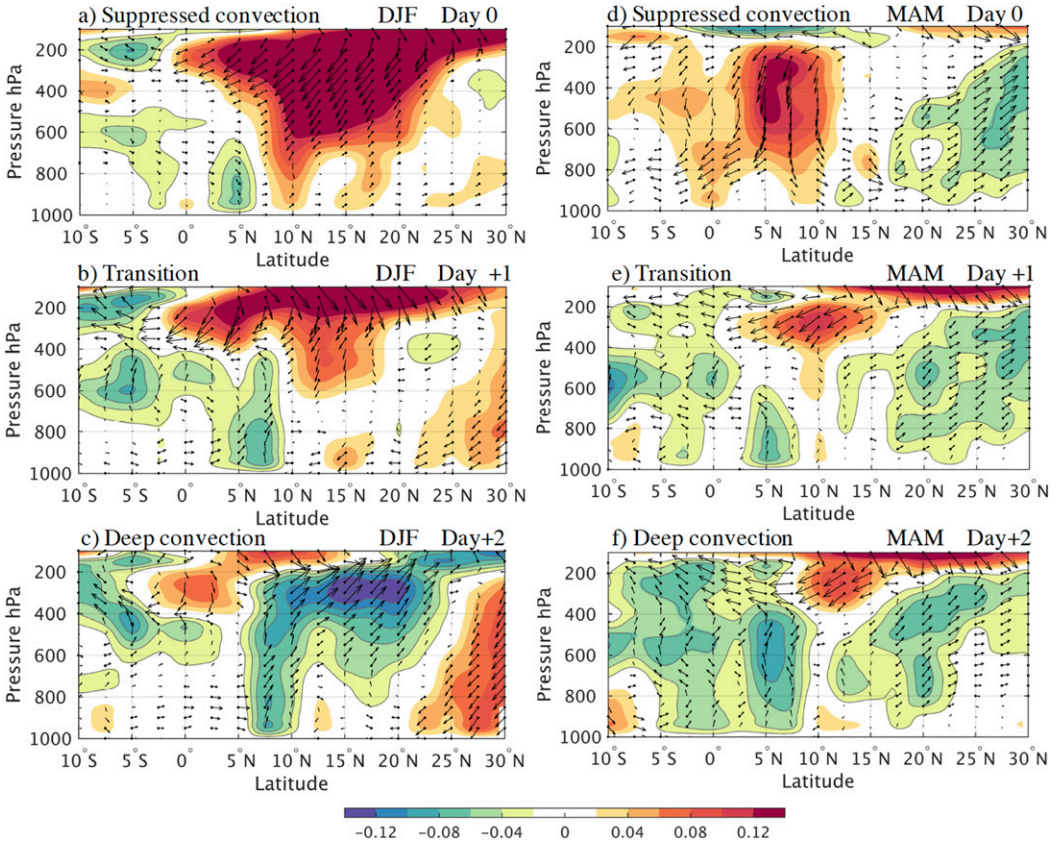

FIG. 13. Latitude–pressure cross sections of omega in Pa s^{-1} (shading) and meridional circulation $\mathbf{v}$, $\boldsymbol{\omega}$ (vectors) anomalies in the far east Pacific (120°W) at different lags for (a)–(c) DJF and (d)–(f) MAM.

injected positive potential vorticity and upper-level divergence in the tropical Kelvin wave along the ITCZ. The evolution of the SMC into a single deep overturning circulation in the southern part of the ITCZ could produce an upper-level outflow and the clouds observed by *CloudSat* between the equator and 5°N.

A weaker, southern branch of the ITCZ is seen at 2.5°S as suggested by the secondary maximum in TRMM rainfall and CLAUS T_b in Fig. 14b. *CloudSat* does not show convective cloud at 2.5°S in Fig. 14d, presumably because of the near-instantaneous, nadir-only view of the radar aboard *CloudSat*. This sampling constraint makes it more likely for *CloudSat* to miss going through convective cells in the less convectively active southern branch of the double ITCZ. In addition, the overpass occurred in the early afternoon, whereas convection maximizes over the east Pacific in the early morning (e.g., Yang and Slingo 2001; Sakaeda et al. 2017). We believe that the double ITCZ may be forced by both the Kelvin wave and extratropical Rossby wave. The scattered shallow clouds seen at 2.5°S in Fig. 14d evolved to deep convection during the following days (not shown) as suggested in Fig. 13f, likely as the result of the strong low-level convergence and upper-level divergence associated with the Kelvin wave and extratropical Rossby wave, respectively.

5. Summary and conclusions

This study analyzes EPDs in the tropical Pacific during boreal winter (DJF) and spring (MAM) when the wave activity in the NH extratropics is strong. Extratropical Rossby waves excited in the NH subtropical jet can propagate to low latitudes and modulate or interact with EPDs in the eastward 2.5–20-day band. We studied the mechanisms of these EPDs over the central and east Pacific using daily T_b and precipitation from satellite data and dynamic fields from MERRA2 reanalysis. We applied EOFs to the eastward 2.5–20-day band T_b and the first principal component is regressed against TRMM precipitation and dynamic fields from MERRA2 at different lags.

The eastward 2.5–20-day band T_b signal is significant during DJF and MAM, especially in the central and east Pacific. During DJF, extratropical NH Rossby waves inject positive PV into the tropics that can initiate and modulate tropical slower moving EPDs. These disturbances propagate

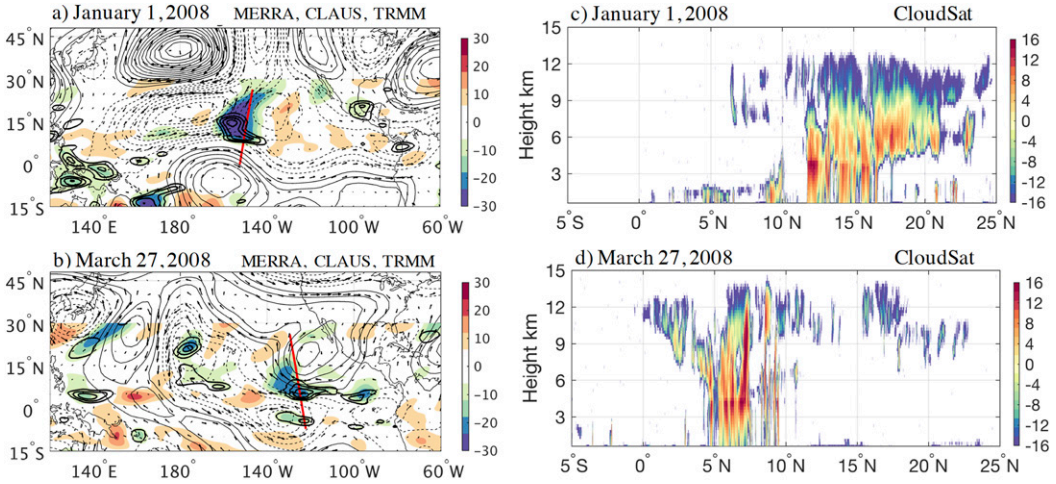

FIG. 14. (a),(b) Eastward 2.5–20-day band T_b in °C (shading), TRMM precipitation in mm day^{-1} (thick contours), 200-hPa streamfunction anomalies in m^2 s^{-1} (contours), and 200-hPa wind vector anomalies in m s^{-1} during a slow-moving EPD on 1 Jan 2008 and a Kelvin wave on 27 Mar 2008, respectively. Largest wind vector is around 40 m s^{-1} and precipitation (streamfunction) contour interval is 0.2 mm day^{-1} (4 m^2 s^{-1}). (c),(d) Nadir swath view of *CloudSat* reflectivity in dB*Z* for each event along the red cross-sectional line.

along 15°N, many degrees north of the climatological ITCZ, with a phase speed around 10 m s^{-1} based on T_b and streamfunction fields. The intrusion of high PV air into low latitudes excites upper-level divergence and midlevel convergence, resulting in deep upper-level cloud decks north of the ITCZ. The upper-level outflow also strengthens the deep meridional circulation in the northern portion of the ITCZ. The climatological SMC observed in the southern part of the ITCZ and below 700 hPa is not significantly impacted by slow-moving EPDs during DJF, perhaps because the extratropical forcing is located in the NH and at upper levels.

During MAM, the strong eastward 2.5–20-day band T_b signal corresponds to Kelvin waves that initiate in the west Pacific and propagate eastward at 15 m s^{-1} along the ITCZ axis. As Kelvin waves reach the central and east Pacific, they may interact with NH extratropical Rossby waves, which propagate eastward at 10 m s^{-1}. The intrusion of high PV air associated with NH extratropical Rossby waves into low latitudes excites upper-level divergence in the Kelvin wave, which strengthens the Kelvin wave convection. The NH Rossby waves in MAM also modulate slower moving EPDs north of the Kelvin waves, around 15°N, similar to DJF. Therefore, tropical convection in the eastward 2.5–20-day band during MAM is the result of Kelvin waves in the ITCZ region (7°N climatologically) and slower moving EPDs north of the ITCZ (15°N climatologically). Shallow convection ahead of the Kelvin wave appears to enhance the SMC in the southern part of the ITCZ.

Our results distinguish between two types of eastward disturbances in the tropical Pacific during DJF and MAM, with different physical mechanisms and impacts in the central and east Pacific ITCZ. Future work involves analyzing the interannual variability of slower moving EPDs and Kelvin waves, especially during El Niño events when the central and east Pacific is dominated by deep convection.

Acknowledgments. The authors thank Juliana Dias for sharing some Matlab scripts to calculate seasonal wavenumber–frequency spectrum, Naoko Sakaeda for providing CLAUS T_b data, and John Nielsen–Gammon for constructive criticism on potential vorticity in the extratropics. The authors also thank Carl Schreck and two anonymous reviewers for their constructive comments that greatly helped to improve the clarity of the manuscript. This work has been supported by NASA Earth and Space Science Fellowship (NESSF) under Grant 80NSSC18K1402P00001.

REFERENCES

Back, L., and C. Bretherton, 2006: Geographic variability in the export of moist static energy and vertical motion profiles in the tropical Pacific. *Geophys. Res. Lett.*, **33**, L17810, https://doi.org/10.1029/2006GL026672.

Baranowski, D. B., M. K. Flatau, P. J. Flatau, and A. J. Matthews, 2016: Impact of atmospheric convectively coupled equatorial Kelvin waves on upper ocean variability. *J. Geophys. Res. Atmos.*, **121**, 2045–2059, https://doi.org/10.1002/2015JD024150.

Bluestein, H. B., 1992: *Synoptic-Dynamic Meteorology in Midlatitudes: Observations and Theory of Weather Systems*. Vol. 2. Taylor & Francis, 594 pp.

Bosilovich, M., R. Lucchesi, and M. Suarez, 2015: MERRA-2: File specification. GMAO Office Note 9 (version 1.0), 73 pp., https://ntrs.nasa.gov/archive/nasa/casi.ntrs.nasa.gov/20150019760.pdf.

Dias, J., S. Leroux, S. Tulich, and G. Kiladis, 2013: How systematic is organized tropical convection within the MJO? *Geophys. Res. Lett.*, **40**, 1420–1425, https://doi.org/10.1002/grl.50308.

Hagos, S., and C. Zhang, 2010: Diabatic heating, divergent circulation and moisture transport in the African monsoon system. *Quart. J. Roy. Meteor. Soc.*, **136**, 411–425, https://doi.org/10.1002/qj.538.

Hodges, K., D. Chappell, G. Robinson, and G. Yang, 2000: An improved algorithm for generating global window brightness temperatures from multiple satellite infrared imagery. *J. Atmos. Oceanic Technol.*, **17**, 1296–1312, https://doi.org/10.1175/1520-0426(2000)017<1296:AIAFGG>2.0.CO;2.

Hoskins, B. J., I. N. James, and G. H. White, 1983: The shape, propagation and mean-flow interaction of large-scale weather systems. *J. Atmos. Sci.*, **40**, 1595–1612, https://doi.org/10.1175/1520-0469(1983)040<1595:TSPAMF>2.0.CO;2.

Huaman, L., and K. Takahashi, 2016: The vertical structure of the eastern Pacific ITCZs and associated circulation using the TRMM precipitation radar and in situ data. *Geophys. Res. Lett.*, **43**, 8230–8239, https://doi.org/10.1002/2016GL068835.

——, and C. Schumacher, 2018: Assessing the vertical latent heating structure of the east Pacific ITCZ using the *CloudSat* CPR and TRMM PR. *J. Climate*, **31**, 2563–2577, https://doi.org/10.1175/JCLI-D-17-0590.1.

Huang, P., and R. Huang, 2011: Climatology and interannual variability of convectively coupled equatorial waves activity. *J. Climate*, **24**, 4451–4465, https://doi.org/10.1175/2011JCLI4021.1.

Huffman, G. J., and Coauthors, 2007: The TRMM Multisatellite Precipitation Analysis (TMPA): Quasi-global, multiyear, combined-sensor precipitation estimates at fine scales. *J. Hydrometeor.*, **8**, 38–55, https://doi.org/10.1175/JHM560.1.

Kiladis, G. N., 1998: Observations of Rossby waves linked to convection over the eastern tropical Pacific. *J. Atmos. Sci.*, **55**, 321–339, https://doi.org/10.1175/1520-0469(1998)055<0321:OORWLT>2.0.CO;2.

——, and K. M. Weickmann, 1992: Extratropical forcing of tropical Pacific convection during northern winter. *Mon. Wea. Rev.*, **120**, 1924–1939, https://doi.org/10.1175/1520-0493(1992)120<1924:EFOTPC>2.0.CO;2.

——, and ——, 1997: Horizontal structure and seasonality of large-scale circulations associated with submonthly tropical convection. *Mon. Wea. Rev.*, **125**, 1997–2013, https://doi.org/10.1175/1520-0493(1997)125<1997:HSASOL>2.0.CO;2.

——, M. C. Wheeler, P. T. Haertel, K. H. Straub, and P. E. Roundy, 2009: Convectively coupled equatorial waves. *Rev. Geophys.*, **47**, RG2003, https://doi.org/10.1029/2008RG000266.

Liebmann, B., G. N. Kiladis, L. M. Carvalho, C. Jones, C. S. Vera, I. Bladé, and D. Allured, 2009: Origin of convectively coupled Kelvin waves over South America. *J. Climate*, **22**, 300–315, https://doi.org/10.1175/2008JCLI2340.1.

Livezey, R. E., and W. Chen, 1983: Statistical field significance and its determination by Monte Carlo techniques. *Mon. Wea. Rev.*, **111**, 46–59, https://doi.org/10.1175/1520-0493(1983)111<0046:SFSAID>2.0.CO;2.

Mapes, B. E., and R. A. Houze Jr., 1995: Diabatic divergence profiles in western Pacific mesoscale convective systems. *J. Atmos. Sci.*, **52**, 1807–1828, https://doi.org/10.1175/1520-0469(1995)052<1807:DDPIWP>2.0.CO;2.

Marchand, R., G. G. Mace, T. Ackerman, and G. Stephens, 2008: Hydrometeor detection using *CloudSat*—An earth-orbiting 94-GHz cloud radar. *J. Atmos. Oceanic Technol.*, **25**, 519–533, https://doi.org/10.1175/2007JTECHA1006.1.

Matsuno, T., 1966: Quasi-geostrophic motions in the equatorial area. *J. Meteor. Soc. Japan*, **44**, 25–43, https://doi.org/10.2151/jmsj1965.44.1_25.

Ortega, S., P. J. Webster, V. Toma, and H.-R. Chang, 2018: The effect of potential vorticity fluxes on the circulation of the tropical upper troposphere. *Quart. J. Roy. Meteor. Soc.*, **144**, 848–860, https://doi.org/10.1002/qj.3261.

Pena-Ortiz, C., D. Gallego, P. Ribera, P. Ordonez, and M. D. C. Alvarez-Castro, 2013: Observed trends in the global jet stream characteristics during the second half of the 20th century. *J. Geophys. Res. Atmos.*, **118**, 2702–2713, https://doi.org/10.1002/JGRD.50305.

Roundy, P. E., and W. M. Frank, 2004: A climatology of waves in the equatorial region. *J. Atmos. Sci.*, **61**, 2105–2132, https://doi.org/10.1175/1520-0469(2004)061<2105:ACOWIT>2.0.CO;2.

Sakaeda, N., G. Kiladis, and J. Dias, 2017: The diurnal cycle of tropical cloudiness and rainfall associated with the Madden–Julian Oscillation. *J. Climate*, **30**, 3999–4020, https://doi.org/10.1175/JCLI-D-16-0788.1.

Schumacher, C., R. A. Houze Jr., and I. Kraucunas, 2004: The tropical dynamical response to latent heating estimates derived from the TRMM Precipitation Radar. *J. Atmos. Sci.*, **61**, 1341–1358, https://doi.org/10.1175/1520-0469(2004)061<1341:TTDRTL>2.0.CO;2.

Stan, C., D. M. Straus, J. S. Frederiksen, H. Lin, E. D. Maloney, and C. Schumacher, 2017: Review of tropical-extratropical teleconnections on intraseasonal time scales. *Rev. Geophys.*, **55**, 902–937, https://doi.org/10.1002/2016RG000538.

Stephens, G. L., and Coauthors, 2002: The *CloudSat* mission and the A-Train: A new dimension of space-based observations of clouds and precipitation. *Bull. Amer. Meteor. Soc.*, **83**, 1771–1790, https://doi.org/10.1175/BAMS-83-12-1771.

Straub, K. H., and G. N. Kiladis, 2002: Observations of a convectively coupled Kelvin wave in the eastern Pacific ITCZ. *J. Atmos. Sci.*, **59**, 30–53, https://doi.org/10.1175/1520-0469(2002)059<0030:OOACCK>2.0.CO;2.

——, and ——, 2003: Extratropical forcing of convectively coupled Kelvin waves during austral winter. *J. Atmos. Sci.*, **60**, 526–543, https://doi.org/10.1175/1520-0469(2003)060<0526:EFOCCK>2.0.CO;2.

Tomas, R. A., and P. J. Webster, 1994: Horizontal and vertical structure of cross-equatorial wave propagation. *J. Atmos. Sci.*, **51**, 1417–1430, https://doi.org/10.1175/1520-0469(1994)051<1417:HAVSOC>2.0.CO;2.

Trenberth, K. E., D. P. Stepaniak, and J. M. Caron, 2000: The global monsoon as seen through the divergent atmospheric circulation. *J. Climate*, **13**, 3969–3993, https://doi.org/10.1175/1520-0442(2000)013<3969:TGMAST>2.0.CO;2.

Vincent, D. G., 1994: The South Pacific convergence zone (SPCZ): A review. *Mon. Wea. Rev.*, **122**, 1949–1970, https://doi.org/10.1175/1520-0493(1994)122<1949:TSPCZA>2.0.CO;2.

Wheeler, M., and G. N. Kiladis, 1999: Convectively coupled equatorial waves: Analysis of clouds and temperature in the wavenumber–frequency domain. *J. Atmos. Sci.*, **56**, 374–399, https://doi.org/10.1175/1520-0469(1999)056<0374:CCEWAO>2.0.CO;2.

Yang, G.-Y., and J. Slingo, 2001: The diurnal cycle in the tropics. *Mon. Wea. Rev.*, **129**, 784–801, https://doi.org/10.1175/1520-0493(2001)129<0784:TDCITT>2.0.CO;2.

Zhang, C., M. McGauley, and N. A. Bond, 2004: Shallow meridional circulation in the tropical eastern Pacific. *J. Climate*, **17**, 133–139, https://doi.org/10.1175/1520-0442(2004)017<0133:SMCITT>2.0.CO;2.

——, D. S. Nolan, C. D. Thorncroft, and H. Nguyen, 2008: Shallow meridional circulations in the tropical atmosphere. *J. Climate*, **21**, 3453–3470, https://doi.org/10.1175/2007JCLI1870.1.